A Multiscale Numerical Study of Hurricane Andrew (1992). Part V: Inner-Core Thermodynamics

DA-LIN ZHANG

Department of Meteorology, University of Maryland at College Park, College Park, Maryland

YUBAO LIU

NCAR/RAP, Boulder, Colorado

M. K. YAU

Department of Atmospheric and Oceanic Sciences, McGill University, Montreal, Quebec, Canada

(Manuscript received 15 October 2001, in final form 15 March 2002)

ABSTRACT

Although considerable progress has been made in understanding the development of hurricanes, our knowledge of their three-dimensional structures of latent heat release and inner-core thermodynamics remains limited. In this study, the inner-core budgets of potential temperature (θ), moisture (q), and equivalent potential temperature (θe) are examined using a high-resolution ($\Delta x = 6$ km), nonhydrostatic, fully explicit simulation of Hurricane Andrew (1992) during its mature or intensifying stage.

It is found that the heat energy is dominated by latent heat release in the eyewall, sublimative–evaporative cooling near the eye–eyewall interface, and the upward surface fluxes of sensible and latent heat from the underlying warm ocean. The latent heating (θ) rates in the eyewall range from less than 10°C h^{-1} to greater than 100°C h^{-1}, depending upon whether latent heat is released in radial inflow or outflow regions. The latent heating rates decrease inward in the inflow regions and become negative near the eye–eyewall interface. It is shown that the radial θ advective cooling in the inflow regions accounts for the initiation and maintenance of the penetrative downdrafts at the eye–eyewall interface that are enhanced by the sublimative-evaporative cooling. It is also shown that the vertical θ advection overcompensates the horizontal θ advection for the generation of the warm-cored eye, and the sum of latent heating and radial advective warming for the development of intense cooling in the eyewall. The moisture budgets show the dominant upward transport of moisture in the eyewall updrafts (and spiral rainbands), partly by the low-level outflow jet from the bottom eye regions, so that the eyewall remains nearly saturated.

The θe budgets reveal that θe could be considered as an approximately conserved variable in the eyewall above the boundary layer even in the presence of deposition–sublimation and freezing–melting. The development of higher-θe surfaces at the eye–eyewall interface is discussed in the context of deep convection, the θe gradient and the mass recycling across the eyewall. It is concluded that the simulated hurricane is thermodynamically maintained by the upward surface flux of higher-θe air from the underlying warm ocean, the descent of higher-θe air in the upper troposphere along the eye–eyewall interface, and the recycling of some warmed-eye air at the eye–eyewall interface.

1. Introduction

The hurricane is a moist vortex whose formation and maintenance rely primarily on the energy transferred from the underlying warm ocean and released as latent heat in convective cells in the eyewall only tens of kilometers across. Although considerable progress has been made in understanding the development of hurricanes, we still have limited knowledge on their three-dimensional (3D) structures and intensity of latent heat release (LHR). We are also uncertain about how LHR is related to the dynamics and thermodynamics in the inner-core regions (Anthes 1982; Liu et al. 1997, 1999; Willoughby 1998). For example, little temperature increase appears in the eyewall where tremendous condensation and precipitation occur. Instead, the eyewall is characterized by intense radial thermal gradients with azimuthal winds decreasing with height. In contrast, a marked warm core always occurs in the eye where there is little diabatic heating. Furthermore, pronounced penetrative downdrafts, distinct from the gentle descent in the eye, develop preferentially in a narrow zone at the

Corresponding author address: Dr. Da-Lin Zhang, Department of Meteorology, University of Maryland at College Park, College Park, MD 20742-2425.
E-mail: dalin@atmos.umd.edu

inner edge of the eyewall where the air is unsaturated, and they are sandwiched between the inside dry-warmer air and the outside moist-colder air (Jorgensen 1984; Liu et al. 1997, 1999; Willoughby 1998). All the above features distinguish hurricanes from any other types of mesoscale convective systems (MCSs) and mesoscale disturbances in the Tropics. To gain a better understanding of these features, it is desirable to examine the thermodynamic budgets in the inner-core regions, particularly the distribution and the intensity of condensation–evaporation that essentially determine the thermodynamic structures and the secondary circulations of hurricanes.

Despite the importance of condensation and evaporation, their magnitudes and 3D distributions could not be measured directly by any remote-sensing and in situ instruments of today. Diabatic heating has often been diagnosed by calculating the residuals of larger-scale heat and moisture budgets (Yanai et al. 1973), the 3D distribution of hydrometeors (Tao et al. 1990), or simply from the profiles of vertical motion in MCSs (Anthes 1982; Puri and Miller 1990; Mapes and Houze 1995). Although many observational budget studies of diabatic heating and moistening have been conducted for tropical and midlatitude MCSs (e.g., Johnson and Young 1983; Kuo and Anthes 1984; Gallus and Johnson 1991; Lin and Johnson 1996), few have been done for hurricanes. Gamache et al. (1993) computed the inner-core hydrometeor water budget of Hurricane Norbert (1984) using retrieved Doppler radar data, and found significant asymmetries in the flux of moisture, condensation, and precipitation. However, they also found that their results are very sensitive to the methods of retrieval used. Much simpler water budget studies were performed by Hawkins and Rubsam (1968) and Hawkins and Imbembo (1976) using the flight-level data taken inside hurricanes. Due to the lack of direct high-resolution observations, these studies could only address very limited aspects of the inner-core thermodynamics of hurricanes.

Recently, some attention has been paid to developing retrieval algorithms to estimate the vertical distributions of rainfall rates and LHR in tropical MCSs (Yang and Smith 1999; Olson et al. 1999) and hurricanes (Olson et al. 1999; Rodgers et al. 1998, 2000) using Special Sensor Microwave Imager (SSM/I) and Tropical Rainfall Measuring Mission (TRMM) microwave imager measurements. In general, these algorithms consist of a cloud model providing the vertical profiles of liquid and frozen hydrometeors, rain fallout rates and vertical derivatives of the liquid–ice mass fluxes; a radiative transfer model calculating microwave brightness temperatures from the model-simulated cloud fields at the SSM/I frequencies/polarizations, and spatially deconvolved SSM/I data. Although these algorithms could capture the basic life cycle of MCSs and reveal some relationship between hurricane intensity and the distribution of precipitation/LHR, there are many uncertainties in estimating the latent heating profiles using satellite measurements. They include low spatial resolution, instrumentation errors, and uncertainties in the modeled cloud fields. Accordingly, satellite-based latent heating profiles require improved resolution and considerable well-designed validation against direct and indirect observations before they could be utilized to examine realistically the inner-core flow structures of MCSs and tropical cyclones.

Alternatively, four-dimensional, high-resolution, dynamically consistent model-simulation datasets could be used to study the 3D structures of latent heating and their effects on hurricane development. Using a quadruply nested-grid ($\Delta x = 5/10/30/90$ km) simulation of a hurricane's eye with parameterized convection, Kurihara and Bender (1982) calculated area-averaged heat budgets in the hurricane eye. They found that the warming and drying by the mean subsidence in the eye tend to be balanced by the cooling and moistening effect of subarea eddies. Their results appeared to be applicable only to the thermodynamics of the eye, and have limited implications for the eyewall convection and hurricane development owing to the crude model physics used. For instance, explicit hydrometeors and grid-scale evaporation were absent in their hurricane model.

The purpose of the present study is to examine the distribution and intensity of condensational/evaporative heating and moistening in the inner-core regions through budgets of potential temperature, moisture, and equivalent potential temperature using a 72-h high-resolution (i.e., $\Delta x = 6$ km), fully explicit simulation of Hurricane Andrew (1992). This simulation, initialized at 1200 UTC 21 August 1992, was performed with a cloud-resolving version of the fifth-generation Pennsylvania State University–National Center for Atmospheric Research (PSU–NCAR) nonhydrostatic Mesoscale Model (MM5). Liu et al. (1997, 1999, hereafter Part I and Part II), have shown that MM5 reproduces reasonably well the track and intensity, as well as the structures of the eye, the eyewall, spiral rainbands, the radius of maximum winds (RMW), and other inner-core features as compared to available observations and the results of previous hurricane studies. In Part III (i.e., Zhang et al. 2000), the vertical force balance was computed from the model output using the inverted 3D perturbation pressure field. It was shown that the subsidence warming in the eye is mechanically driven by rapid rotation of the eyewall, just like the change in shape of a free surface associated with a rotating vessel filled with water. In the present study, we will investigate (a) the 3D distribution and intensity of the (condensation–evaporation, freezing–melting, deposition–sublimation) heating and moistening in the eyewall; (b) their balanced thermodynamics in relation to the secondary circulations in the inner-core regions; (c) the sources and transport of equivalent potential temperature aiding in the development of the eyewall convection; and (d) the significance of radial thermal advection and evaporation in the

inflow regions in driving the penetrative downdrafts at the inner edge of the eyewall.

The next section presents budget equations of the heat, moisture, and equivalent potential temperature along with the inner-core axisymmetric structures of the simulated Andrew. Sections 3–5 describe, respectively, the budgets of heat, moisture, and equivalent potential temperature during the mature stage of the storm. A summary and conclusions are given in the final section.

2. Budget equations and inner-core structures

The budget equations of heat and moisture presented herein are based on the governing equations used in MM5 (see Dudhia 1993; Grell et al. 1995). All the MM5's prognostic variables are written in the mass-weighted (i.e., $p^* = p_s - p_t$) flux form in (x, y, σ) coordinates (on a Mercator map projection), with p_s and p_t being the pressure at the bottom and the top of the model, respectively. Because of the dominant axisymmetric structures of hurricanes, we will discuss the budgets and inner-core features in the cylindrical coordinate system (r, λ, z), where r is the radius pointing outward from the minimum surface pressure of the vortex. Interested readers are referred to Part II for a detailed description of the transformation between the MM5 (x, y, σ) and cylindrical coordinates.

The governing equations in cylindrical coordinates for the specific humidity q, the potential temperature θ, and the equivalent potential temperature θe are

$$\frac{dq}{dt} = -(q_{\rm CON} - q_{\rm CEV} - q_{\rm REV} + q_{\rm DEP} - q_{\rm SUB}) + q_{\rm BLD}, \quad (1)$$

$$\frac{d\theta}{dt} = \frac{L_v}{C_p}\pi(q_{\rm CON} - q_{\rm CEV} - q_{\rm REV}) + \frac{L_f}{C_p}\pi(q_{\rm FRZ} - q_{\rm MLT}) + \frac{L_s}{C_p}\pi(q_{\rm DEP} - q_{\rm SUB}) + \theta_{\rm RAD} + \theta_{\rm BLD}, \quad (2)$$

$$\frac{d\theta_e}{dt} = \left[\frac{L_f}{C_p}\pi(q_{\rm FRZ} - q_{\rm MLT} + q_{\rm DEP} - q_{\rm SUB})\right] \times \exp\left(\frac{L_v q}{C_p T_L}\right) + \theta{\rm e}_{\rm RAD} + \theta{\rm e}_{\rm BLD}, \quad (3)$$

where

$$\pi = (p_0/p)^{R/C_p}, \quad (4)$$

$$\frac{d}{dt} = \frac{\partial}{\partial t} + U\frac{\partial}{\partial r} + \frac{V}{r}\frac{\partial}{\partial \lambda} + W\frac{\partial}{\partial z}, \quad (5)$$

W, U, and V are the respective vertical, radial, and azimuthal winds relative to the moving storm center; L_v, L_f, and L_s are the latent heat of condensation, fusion, and sublimation, respectively; T_L is the temperature at the lifting condensation level calculated using Bolton's (1980) formula. The subscripts, BLD and RAD, represent the contributions associated with the maritime boundary layer (MBL) and diffusive effects, and the cloud–radiation interaction, respectively. All the other symbols assume their usual meteorological meaning. See Part I and Tao and Simpson (1993) for more detailed description of the physical processes used in Eqs. (1)–(3). Note that the storm-relative flow is used in Eq. (5) to compute the horizontal advection in order to separate the advective effects associated with the storm movement from the dynamical processes that influence the storm development.

For the convenience of budget descriptions, we group the rates of condensation ($q_{\rm CON}$), evaporation of cloud droplets ($q_{\rm CEV}$) and raindrops ($q_{\rm REV}$), deposition ($q_{\rm DEP}$) and sublimation ($q_{\rm SUB}$) of ice particles into the net in-cloud moisture source term $q_{\rm CLD}$; and the total rates of LHR, including the freezing of raindrops ($q_{\rm FRZ}$) and the melting of snow and graupel ($q_{\rm MLT}$), into the net in-cloud heat source term $\theta_{\rm CLD}$. That is,

$$q_{\rm CLD} = q_{\rm CON} - q_{\rm CEV} - q_{\rm REV} + q_{\rm DEP} - q_{\rm SUB}, \quad (6)$$

$$\theta_{\rm CLD} = \frac{L_v}{C_p}\pi q_{\rm CLD} + \frac{L_f}{C_p}\pi(q_{\rm FRZ} - q_{\rm MLT} + q_{\rm DEP} - q_{\rm SUB}), \quad \text{and} \quad (7)$$

$$\theta{\rm e}_{\rm CLD} = \left[\frac{L_f}{C_p}\pi(q_{\rm FRZ} - q_{\rm MLT} + q_{\rm DEP} - q_{\rm SUB})\right] \times \exp\left(\frac{L_v q}{C_p T_L}\right). \quad (8)$$

Note that the sum of $\theta_{\rm CLD} + \theta_{\rm RAD} + \theta_{\rm BLD}$ (and $\theta{\rm e}_{\rm CLD} + \theta{\rm e}_{\rm RAD} + \theta{\rm e}_{\rm BLD}$) represents the only sources/sinks of thermodynamic energy in Eq. (2) [and Eq. (3)], since θ (and θe) is a conserved variable in an otherwise invisid, adiabatic (and pseudoadiabatic) flow.

In order to obtain the budgets of θ and θe as accurately as possible, all the terms in Eqs. (1)–(8) are derived directly from the model output without any approximation in calculating their associated derivatives. For example, the θ and θe gradients or their time rates are calculated from

$$\nabla\theta = T\nabla\pi + \pi\nabla T, \quad \text{and} \quad (9)$$

$$\nabla\theta{\rm e} = \left[\nabla\theta + \frac{L_v\theta}{C_p T_L}\left(\nabla q - \frac{q}{T_L}\nabla T_L\right)\right]\exp\left(\frac{L_v q}{C_p T_L}\right), \quad (10)$$

where π and its derivative are obtained by including the perturbation pressure, which is one of the MM5 prognostic equations. All the other details in budget calculations are the same as those described in Part III and IV of this series of papers (i.e., Zhang et al. 2000, 2001). Specifically, the model integration data are output over the fine-mesh domain at 5-min intervals from the 56–

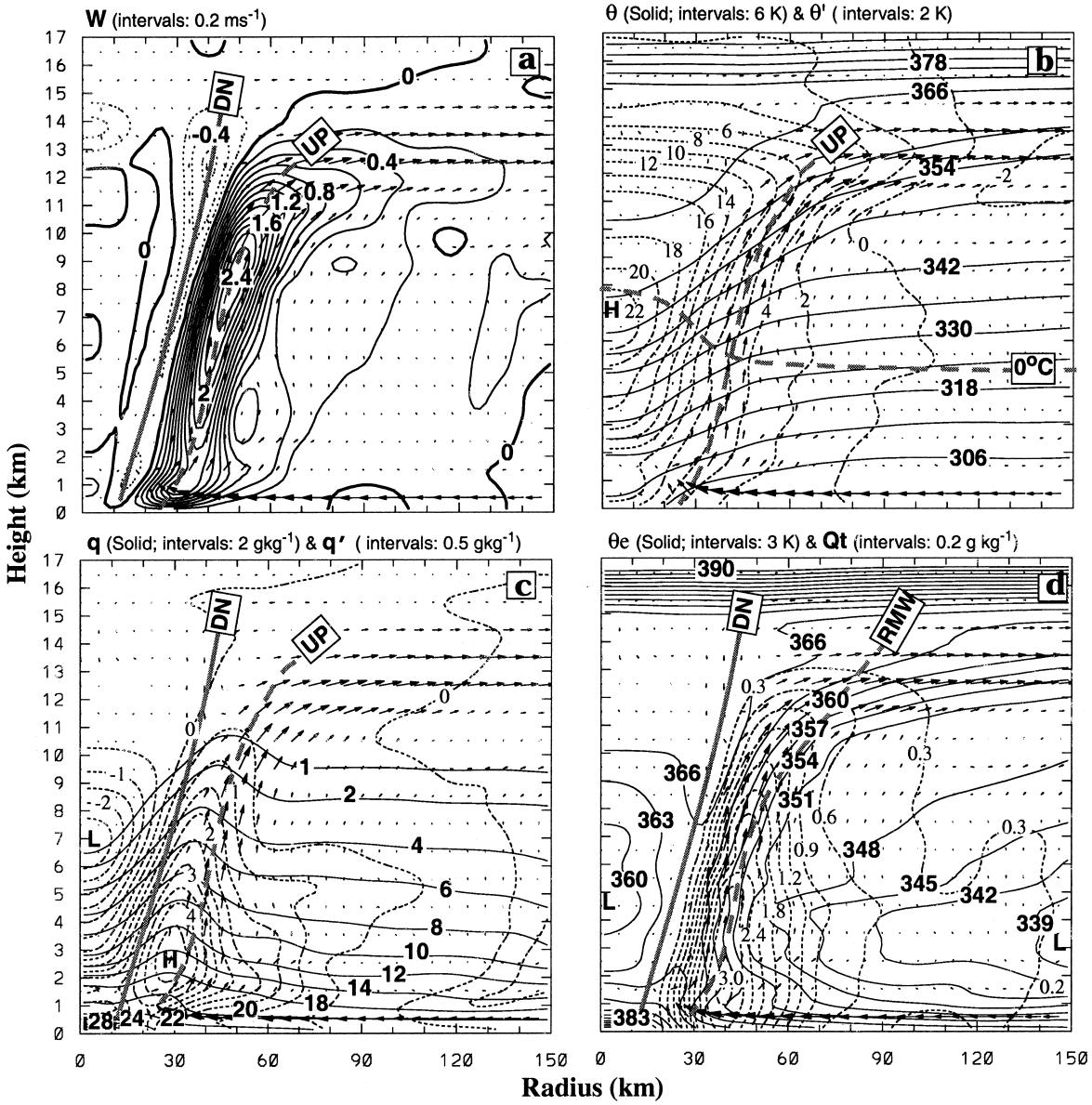

FIG. 1. The radius–height cross sections of the hourly and azimuthally averaged fields: (a) vertical velocity (W, every 0.2 m s^{-1}); (b) the potential temperature (θ, solid; every 4 K) and its deviations (θ', dashed; every 2 K); (c) specific humidity (q, solid; every 2 g kg^{-1}) and its deviations (q', dashed; every 0.5 g kg^{-1}); and (d) the equivalent potential temperature (θe, solid; every 3 K) and total cloud hydrometeors (Qt, dashed; every 0.3 g kg^{-1}), which are taken from the 56–57-h integration valid between 2000–2100 UTC 23 Aug 1992. They are superposed with the cross-sectional flow vectors, the axes of the eyewall updraft (UP), the inner-edge dry downdraft (DN) and the RMW. Letters H and L denote the local max and min, respectively.

57-h integration, valid at 2000–2100 UTC 23 August 1992. At this time, the storm has entered its mature stage with a maximum surface wind of 68 m s^{-1} but is still intensifying at a rate of 1 hPa h^{-1} (see Fig. 2 in Part I). *Each budget term,* rather than each variable, is then transformed from the model coordinates to cylindrical coordinates with the center of the storm at the origin. For most of the results presented here, each budget term is averaged azimuthally (for each 5-min dataset) and temporally over the 1-h period. With the azimuthal average, we may neglect the azimuthal advection terms in all the budget equations. Nevertheless, such azimuthal averages are statistically less meaningful near the center of the hurricane due partly to the use of fewer samples and partly to the inconsistency between the pressure and circulation centers in the mid- to upper troposphere.

For the convenience of subsequent discussions, Fig. 1 shows the azimuthally and temporally averaged radius–height cross sections of vertical motion, θ and its deviation, q and its deviation, θe and total hydrometeors

Qt. All deviations are obtained by subtracting their azimuthally and radially averaged values at individual heights. The eyewall is basically characterized by intense slantwise updrafts that are fed by an inflow within the MBL. At the top of the eyewall, some air mass returns to the eye (cyclonically) and descends all the way to the MBL at the inner edge of the eyewall (Fig. 1a), as defined in Part II as dry downdrafts (DN). Weak descent dominates the eye region. The θ field shows an intense warm core in the eye with a maximum warm anomaly of over 22°C at $z = 7$ km (Fig. 1b). The averaged radial θ gradient across the eyewall amounts to about 18°C/50 km. Of interest is that the ridge axis of the warm anomaly tilts upward from the core to the upper portion of the upper-outflow layer, with a slope close to the $\theta = 362$ K surface. This appears to suggest that the warm-cored structure is somehow produced by the subsiding air associated with the returning air mass that descends cyclonically in a spiral manner along the isentropic surface inward from the DN zone (cf. Fig. 6c in Liu et al. 1999 and Fig. 1b herein). This point will be substantiated by thermodynamic budgets in the next section. In the MBL, θ increases toward the lower pressure as a result of the upward transport of surface sensible heat.

The averaged axisymmetric moisture field shows typically moist air in the eyewall and dry air in the eye (Fig. 1c). Of interest is that the moist core and its anomaly axis do not coincide with the updraft core (UP) but appear near the inner edge of the eyewall, producing marked moisture gradients in the eye. Given the near-saturated conditions in the eyewall updrafts, this moist core is apparently related to warmer temperatures at the inner edge. On the other hand, the axis of cloud hydrometeors is closely oriented along that of the eyewall updrafts, except below the peak concentration level (i.e., $z = 3$ km) where evaporation of rainfall particles increases toward the surface (see Fig. 1d). The vertical structure of cloud hydrometeors differs more from that of vertical motion in a column due to the fallout of rainwater and snow. Note the significant increase in water vapor content toward the storm in the MBL that results clearly from the upward fluxes of surface moisture. The most moist air (>25 g kg^{-1}) appears at the center of the eye (Fig. 1c). Similarly, θe in the MBL increases toward the eyewall with a particularly high (>383 K) value at the eye center (Fig. 1d). The air–sea interaction processes help to maintain the potential instability in the storm environment and feed energy to the eyewall convection. Note also the downward dip of higher θe ($=366$ K) at the upper level and the upward tilt of the high-θe axis near the inner edge of the eyewall that are caused by the downward advection of higher-θe (or potentially warmer, i.e., roughly $\theta = 366$ K) air in the DN zone from the upper troposphere (cf. Figs. 1b and 1d) and by the upward transport of higher-θe air through the MBL processes and weak updrafts from the bottom of the eye into the eyewall, respectively. These features have been partially observed (Hawkins and Imbembo 1976), and clearly shown in Part I; the related mechanisms will be further discussed in section 5.

3. Potential temperature θ budgets

In this section, we examine the 3D heat budgets of Eq. (2) in the inner-core regions of the simulated Andrew. It is apparent from Fig. 2 that the heat energy source/sink is dominated by LHR in the eyewall, sublimative–evaporative cooling at the eye–eyewall interface (i.e., along the DN axis) and the upward surface fluxes of sensible (and latent) heat from the underlying warm ocean. The azimuthally averaged slantwise LHR structure in the inner-core region is similar to that of vertical motion (cf. Figs. 1a and 2b), which is consistent with the notion that the eyewall updrafts are mostly driven by LHR. The peak LHR rate, which is over 45°C h^{-1}, occurs at $z = 7$ km that is slightly below the level of the updraft core. Despite such an intense heating rate, little (azimuthally averaged) buoyancy could be noted in the eyewall (see Part III), since the averaged ascending parcels are warmer than the air outside but colder than the air inside. In the absence of buoyancy, lifting of air parcels in the eyewall could only be provided by the dynamically induced vertical pressure gradient force (see Part III). Figures 2b–d show that most of the latent heating is generated by condensation in the eyewall. While depositional growth and freezing are secondary in determining the vertical heating profiles, they tend to shift the heating maximum to a slightly higher level and the heating effects into a deeper layer (see Figs. 2c,d).

Of interest is a narrow zone of pronounced sublimative–evaporative (>4°C) cooling that coincides with downdrafts along the DN axis (cf. Figs. 1a and 2b), extending from the descending return flow at $z = 13$ km down to the MBL. This zone of cooling clearly facilitates the intensification of downdrafts at the eye–eyewall interface. Latent cooling is also present inside the storm and in the storm environment. For example, melting of snow and graupel produces marked (>4°C h^{-1}) cooling rates below the 0°C isotherm from the eyewall to its outer environment, coinciding with the development of a shallow layer of weak mesoscale convergence (cf. Fig. 2d herein and Fig. 1b in Part IV). A sensitivity experiment, in which ice phase was turned off from the control simulation, indicates that the simulated hurricane is 8–10 hPa stronger than the control one at the end of the 72-h integration (not shown), suggesting the importance of the sublimative and melting cooling in suppressing the storm. This is similar to that discussed by Zhang (1989) in association with the development of a midlevel mesovortex. The evaporative cooling rates, peaked in the MBL near the outer edge of the eyewall, range between 1–3°C h^{-1}. The MBL cooling rates are overcompensated by the upward sur-

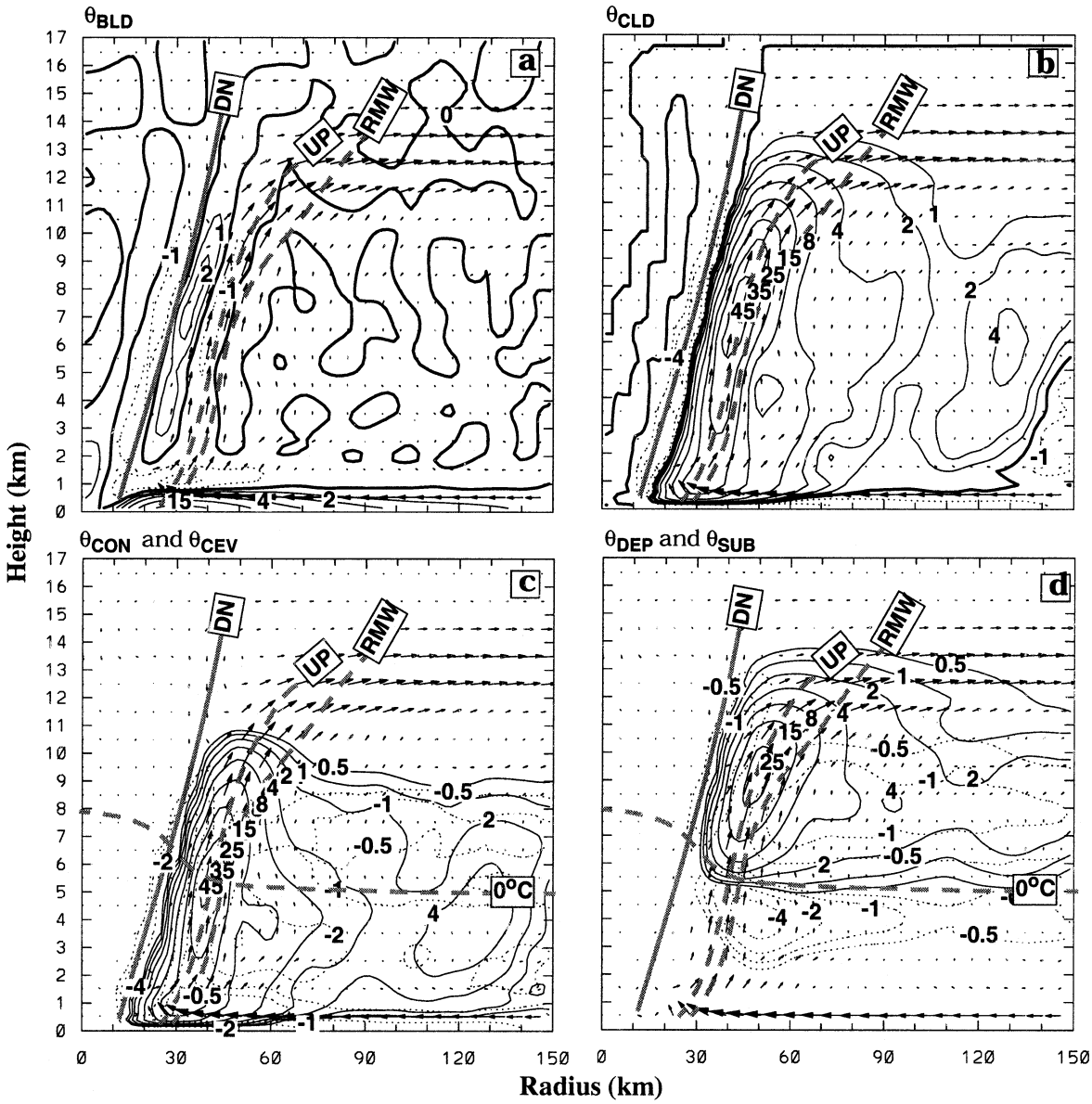

FIG. 2. As in Fig. 1 but for the potential temperature θ sources/sinks: (a) the PBL and diffusive heating rates (θ_{BLD}); (b) total in-cloud heating rates (θ_{CLD}); (c) in-cloud condensational heating (θ_{CON}, solid) and evaporative cooling (θ_{CEV}, dashed) rates; and (d) in-cloud deposition/freezing heating (θ_{DEP}, solid) and sublimative/melting cooling (θ_{SUB}, dashed lines) rates that are contoured at 0, ±0.5, ±1, ±2, ±4, ±8, ±15, ±25, ±35, and ±45 K h^{-1}. (a), (b) Solid (dashed) lines are for positive (negative) values.

face sensible heat flux whose magnitude is highly dependent on the surface wind speeds, for example, greater than 15°C h^{-1} near the RMW (cf. Figs. 2a and 2b). Including the radiative cooling (warming) above (below) the cloud layer affects little of the total diabatic heating, since it is even weaker than the diffusive effects shown in Fig. 2a. However, the cloud–radiation interaction plays an important role in the deepening of the cyclonic storms when numerical models are integrated for more than 24 h (Krishnamurti et al. 1991; Zhang and Bao 1996). Without it, the simulated Andrew would be 8–10 hPa weaker than the control one due to the destabilizing effect of radiative cooling at the MBL cloud top (not shown).

Figure 3 shows the roles of the radial and vertical θ advections in redistributing the intense diabatic heating in the inner-core regions. Because of the intense radial thermal (and θe) gradient, the deep radial outflow, which is supergradient (see Part IV), tends to advect warmer (higher θe) air in the core regions to strengthen the eyewall updrafts (Fig. 3a), thereby weakening the thermal gradient across the eyewall. The warm advective rates near $z = 10$ km are as intense as 15°–18°C h^{-1}, which exceed the local diabatic heating rates (cf.

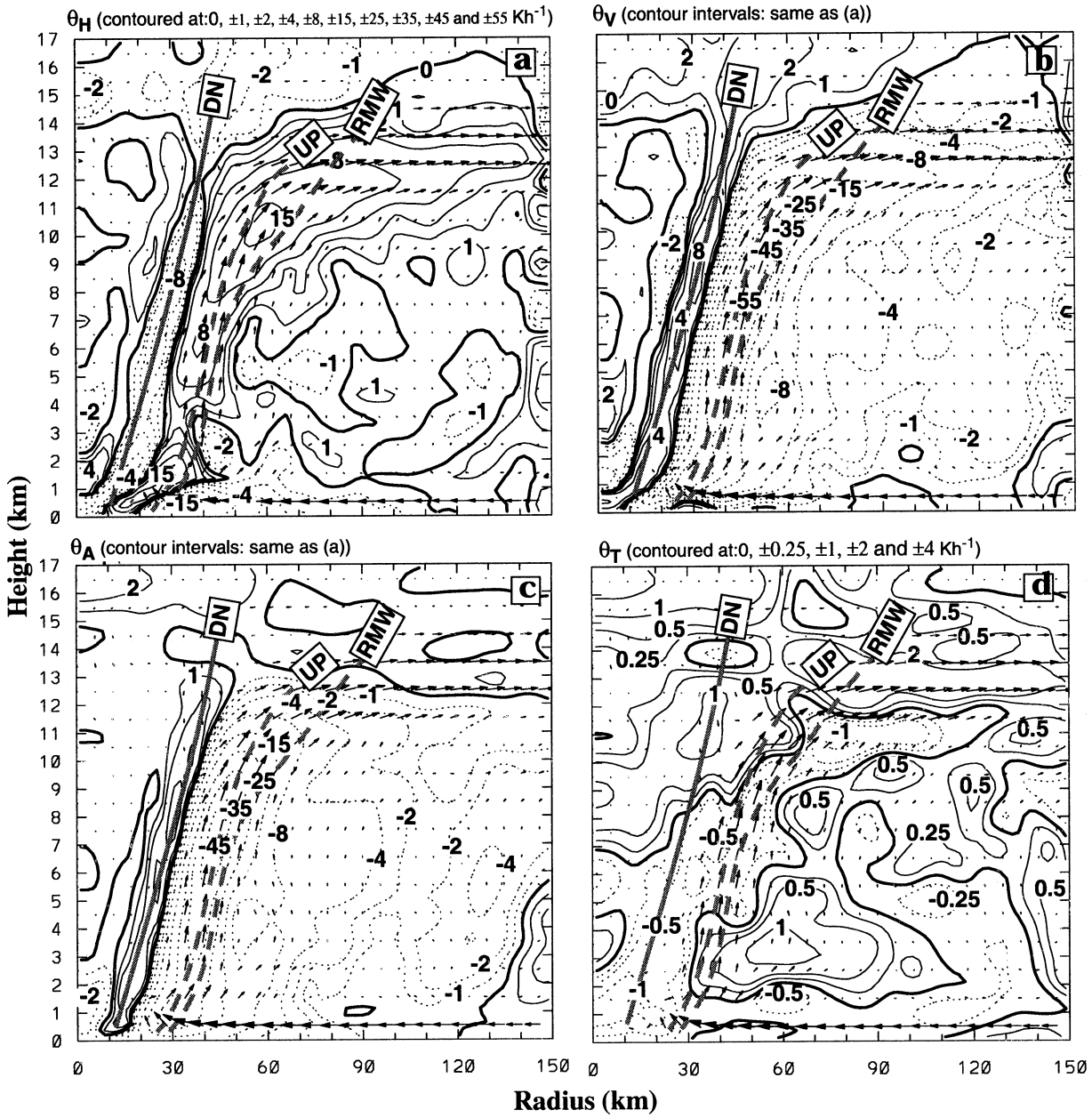

FIG. 3. As in Fig. 1 but for (a) the horizontal advection (θ_H); (b) the vertical advection (θ_v); (c) the total advection (θ_A); and (d) the local tendency (θ_T) of potential temperature. Solid (dashed) lines are for positive (negative) values.

Figs. 3a and 2b). The low-level outflow jet (LLOJ) also provides pronounced radial warm advection (>15°C h^{-1}) to feed the eyewall updrafts. The slantwise inward, descending flow along the DN axis, as shown in Part II, produces cooling but it is offset significantly by the warming associated with descent (Fig. 3c). Nevertheless, *the radial advective cooling in the upper inflow regions appears to account for the initiation of the penetrative downdrafts above the upper outflow layer and their maintenance below along the DN axis,* since its magnitude is nearly twice as large as the evaporative cooling (cf. Figs. 3a and 2b). Convergence of the air mass into the DN flow leads to an inward-slanted zone (i.e., next to the DN zone) of radial warm advection and vertical advective cooling in the eye.

In comparison, the vertical advection produces substantially *intense* adiabatic cooling in the eyewall and weak cooling in the outer rainband region (Fig. 3b). The peak cooling rate in the updraft core is over 55°–60°C h^{-1} at z = 9 km, which offsets more than the total diabatic heating (cf. Figs. 3b and 2b). This appears to explain why little net warming can be found in the eye-

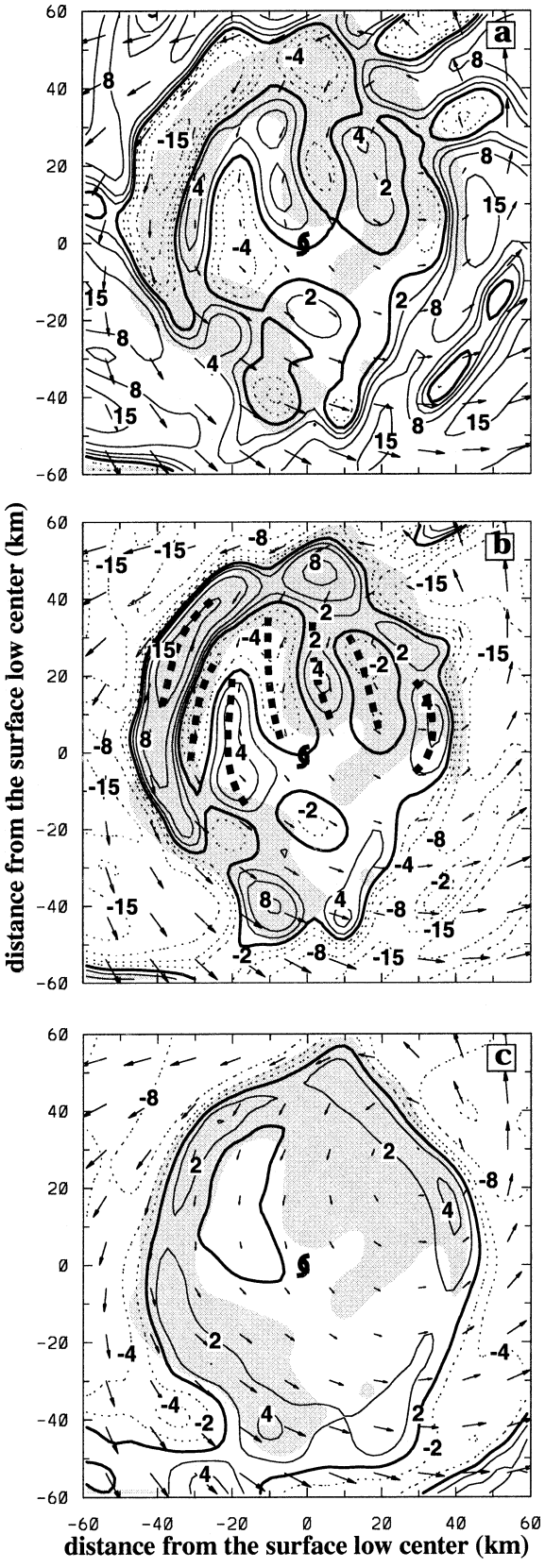

wall in the presence of intense LHR. In particular, the adiabatic cooling associated with the eyewall updrafts gives rise to intense gradients in the cooling rate from the inner edge to the core of the eyewall. On the other hand, the eye region experiences slow subsidence warming, though influenced by the propagation of internal inertial-gravity waves (see Part II).

Of importance is that the total thermal advection rates are similar in pattern but opposite in sign to the diabatic heating rates (cf. Figs. 3c and 2b). This reveals a near-balanced relationship between the total θ advection and diabatic heating in storm-relative framework. Thus, the local θ changes in the eyewall are basically small residues among the large terms (Fig. 3d); they are clearly too small to be detected observationally. For instance, the simulation exhibits less than 1°C h^{-1} cooling rates in the eyewall with slight (advective) warming in the upper outflow layer. Although the local θ changes in the eye are also small, one can see a general adiabatic warming above $z = 7$ km and oscillatory cooling/warming below. (Such oscillations near the vortex center are statistically less significant compared to the azimuthal averages away from the center.) Despite the small amplitudes, the general net warming in the eye and cooling in the eyewall, both dominated by the vertical advections, are consistent with the development and strengthening of a warm-cored eye and intense thermal gradients across the eyewall (cf. Figs. 1b and 3d). Based on the above results, we may state that *the vertical thermal advection accounts for cooling of the eyewall with the maximum in the updraft core and a warm core in the eye such that the thermal gradient across the eyewall increases with time, whereas the radial thermal advection tends to reduce the thermal gradient.*

Of interest is that a net warming ridge axis tilts upward from the eye center near $z = 9$ km; this coincides closely with the θ-perturbation ridge axis or $\theta = 362$ K surface (cf. Figs. 3d and 1b). This result confirms the conjecture given in section 2 that a significant portion of the subsidence warming in the eye, caused by the rotating eyewall (see Part III), is associated with the descending air mass along the DN axis from the return inflow above the upper outflow layer. Fig. 4 shows that the warming occurs in association with an inertial-gravity wave mode. Specifically, the (cyclonic) return inflow converges at the DN region and begins to descend as a result of (inward) advective and sublimative cooling, inducing inertial-gravity waves in the eye. In the present

←

FIG. 4. Horizontal distribution of the hourly averaged (a) horizontal advection (θ_H); (b) vertical advection (θ_v); and (c) total advection ($\theta_H + \theta_v$) of potential temperature (solid: positive, dashed: negative) superposed with in-plane flow vectors at $z = 12$ km. They are contoured at 0, ±2, ±4, ±8, and ±15 K h^{-1}, and taken from the 56–57-h integration valid between 2000–2100 UTC 23 Aug 1992. Areas of downward motion are shaded. Labels on the frame denote the distance (km) from the min surface pressure.

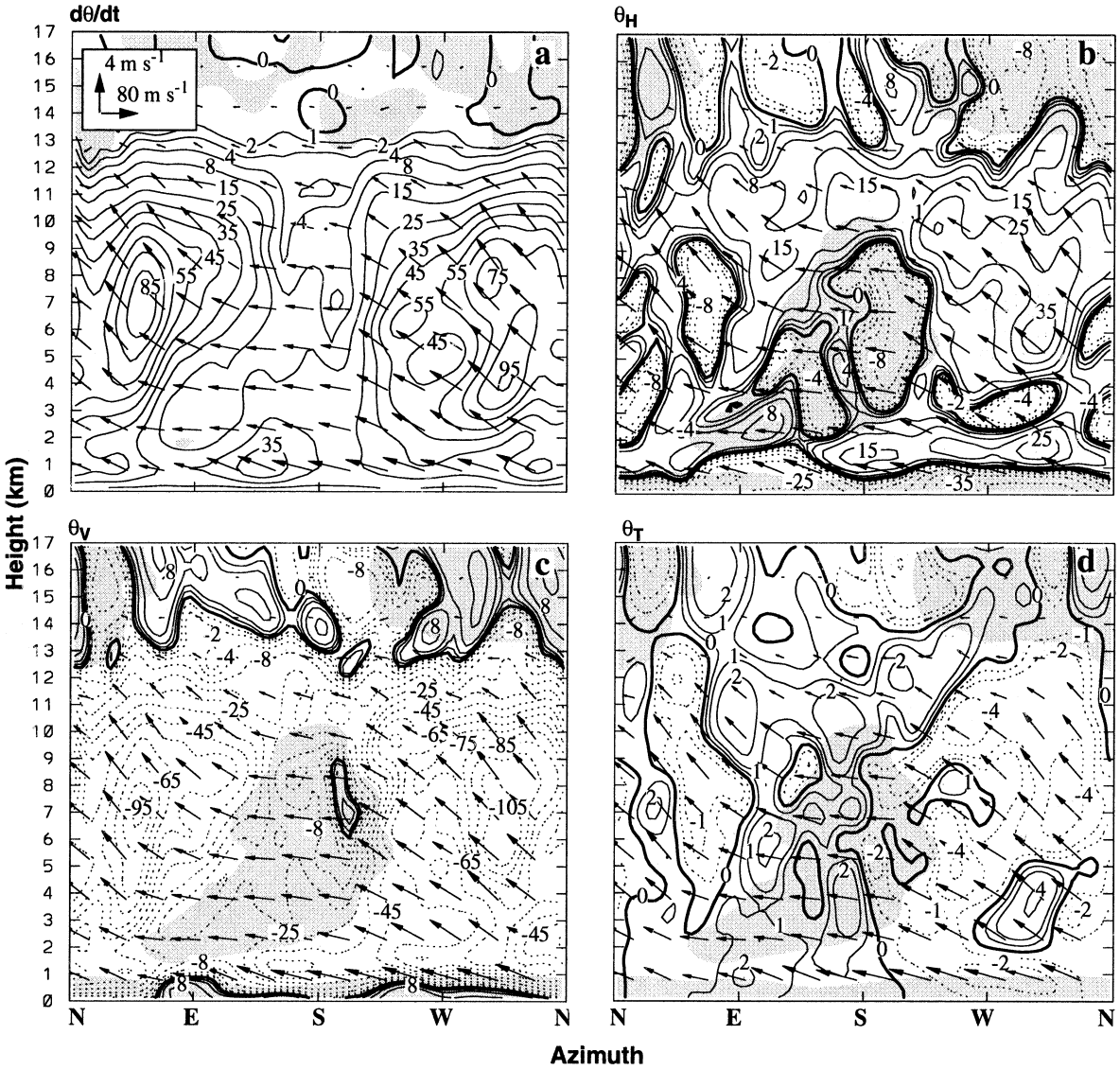

FIG. 5. The height–azimuth cross sections of the temporally averaged potential temperature θ budgets: (a) the total diabatic heating rates ($d\theta/dt$); (b) horizontal advection (θ_H); (c) vertical advection (θ_v); and (d) local tendency (θ_T) that are taken along a *slanting surface* in the eyewall (i.e., from $R = 30$ km at the surface to $R = 70$ km at the 17-km height), superposed with in-plane flow vectors. They are contoured at 0, ±1, ±2, ±4, ±8, ±15, ±25, ±35, ±45, ±55, ±65, ±75, ±85, ±95, and ±105 K h^{-1}, and taken from the 56–57-h integration valid between 2000–2100 UTC 23 Aug 1992. (a) Shadings denote areas of downdrafts; (b)–(d) Shadings denote areas of the system-relative radial inflows. Solid (dashed) lines are for positive (negative) values.

case, several waves are evident in the eye region even after temporal averaging, as shown by the vertical and horizontal advective warming/cooling rates in Figs. 4a,b (refer to Part II for the radial propagation of inertial-gravity waves). Similar wave activities can also be seen from the instantaneous vertical motion field (not shown). In spite of the wavy structures, the net advective effects are to warm the eye and build up the warm core (cf. Figs. 4c and 1b), thereby leading to the lowering of the central pressure. Zhang and Fritsch (1988) showed that surface pressure changes are more sensitive to warming at the upper levels than at the lower levels.

The slanting height–azimuth cross sections of heat budgets through the sloping updraft core are given in Fig. 5, which shows the asymmetric heating and advective structures in the eyewall. The total diabatic heating occurs everywhere in the eyewall, and it is highly asymmetric with the peak rate (>95°C h^{-1}) being twice larger than its axisymmetric value (cf. Figs. 2b and 5a). In general, the diabatic heating magnitude depends on whether the eyewall updrafts are in the inflow or outflow regions, given the intense thermal gradients across the eyewall (see Fig. 1b). That is, radial inflows above the MBL tend to advect the environmental colder (and also drier) air into the core, suppressing the updrafts and LHR (cf. Figs. 5a,b). By comparison, radial outflows

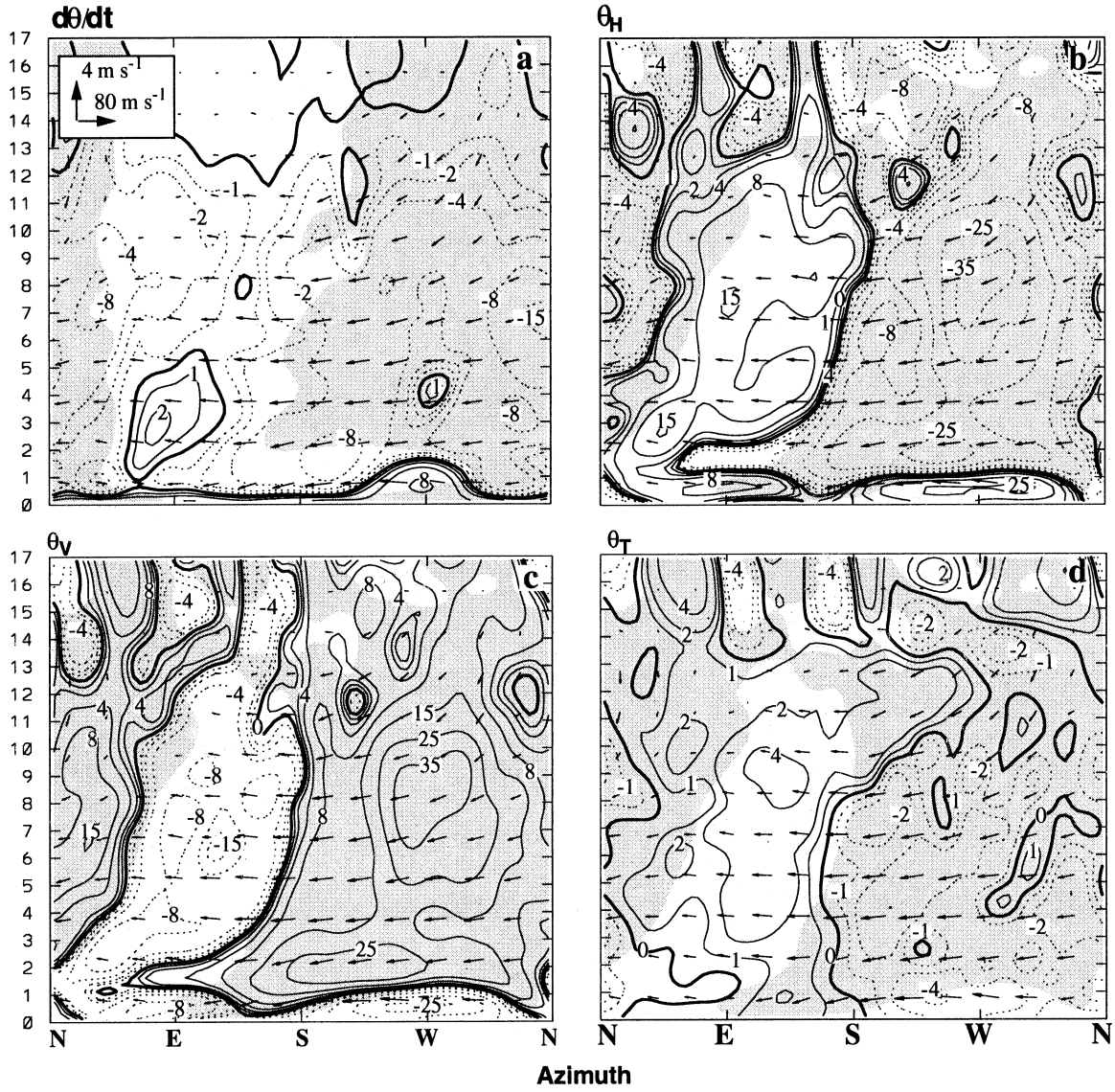

FIG. 6. As in Fig. 5 but taken along a slanting surface through the core of the inner-edge dry downdraft (i.e., from $R = 15$ km at the surface to $R = 50$ km at $z = 17$ km).

cause warm (and higher θe) advection that helps to intensify the updrafts and thus LHR in the eyewall. Thus, the midlevel diabatic heating rates vary from 10°–15°C h^{-1} in the inflow regions to 85°–95°C h^{-1} in the outflow regions. As expected, the intensifying updrafts in the outflow regions produce adiabatic cooling rates that are higher than those in the inflow regions (Fig. 5c). The intense adiabatic cooling in most of the updraft core, peaked at a rate of over 105°C h^{-1}, overcompensates for the sum of diabatic heating and horizontal advective warming, although the net local cooling tendencies are one order of magnitude smaller than the diabatic heating rates (Fig. 5d). Only in the inflow regions, the relatively weak diabatic heating dominates the total advective cooling, leading to weak warming rates (i.e., 1°–2°C h^{-1}). Since *these inflows and outflows are associated with the radial and azimuthal propagation of vortex-Rossby waves*, as discussed in Part IV, the distribution and magnitude of LHR in the eyewall may need to be understood in the context of vortex-Rossby waves (Montgomery and Kallenbach 1997; Chen and Yau 2001).

In contrast, the relative roles of heat budgets at the inner edge of the eyewall are opposite in sign to those in the eyewall. As mentioned earlier, the DN region experiences latent cooling due to the evaporation of cloud hydrometeors from the eyewall into the eye's dry air; the cooling rates are several times greater in the inflow regions than that in the outflow regions (Fig. 6a). Of significance is that the advective heating/cooling

rates are much greater than the diabatic rates, particularly in the upper levels. For example, horizontal advection associated mostly with radial inflows produces a cooling rate of >35°C h^{-1}, which is about 2–3 times greater than the local diabatic cooling rate (cf. Figs. 6a,b). This reveals further that the horizontal advective cooling not only initiates the descent of the return inflow near DN above the upper outflow layer, but also accounts for the maintenance of the penetrative downdrafts. We acknowledge that the penetrative downdrafts were speculated in our earlier papers as being forced only by the evaporative cooling. Evidently, *they are dynamically driven by radial inflows in the presence of intense thermal gradients across the eyewall and then thermodynamically enhanced by the sublimative–evaporative cooling resulting from the inward advection of cold cloudy air into the warm-dry eye region.* On the other hand, the downdraft developments tend to enhance the radial inflow, based on the principle of conservation of mass. Because of less moisture available for evaporation further inward in the inflow air, this (cyclonically) descending air must move isentropically, contributing to the warmth of the eye core (Fig. 1b).

Note that in the western semicircle the horizontal advective cooling is distributed in the DN region but advective warming appears in the eyewall (cf. Figs. 5b and 6b). This is closely related to the highly divergent radial flows at the inner edge of the eyewall (e.g., see Fig. 3g in Part II). In the DN outflow region, the advective warming rates are similar both in sign and in magnitude to those in the eyewall. Nevertheless, the horizontal advective cooling (warming) in DN is almost offset by the vertical advective warming (cooling) (cf. Figs. 6b and 6c). As a result, the net θ tendencies in the DN region exhibit weak cooling (warming) in the inflow (outflow) regions—a wavenumber-1 structure similar to that of the radial flows (see Fig. 6d).

Figure 7 shows horizontal maps of heat budgets at $z = 8$ km where the intensity of eyewall updrafts is peaked. In spite of the temporal averaging, the general distributions of evaporative cooling in the outer region, intense diabatic heating in the eyewall, evaporative cooling at the inner edge of the eyewall and little warming (due to radiative and diffusive processes) in the eye are evident (Fig. 7c). The wave signals in the eye are much less than those in the upper levels (cf. Figs. 4a,b and 7a,b). Of importance is that the banded intense evaporative cooling in DN occurs side by side with the banded intense LHR in the eyewall, accounting for the pronounced (radial) divergent flows at the eye–eyewall interface. These divergent flows give rise to horizontal advective (outflow) warming in the eyewall and (inflow) cooling in DN (Fig. 7a). In the southeastern quadrant where the *eyewall* heating is relatively weak, however, more warm air in the *eye* (>15°C h^{-1}) is being transported outward by supergradient flows. Moreover, this horizontal advective warming overcompensates the upward adiabatic cooling in this quadrant of the eye (cf. Figs. 7a,b,d). Elsewhere in the eyewall, the upward adiabatic cooling exceeds the combined horizontal advective and latent heating, whereas in the DN and eye regions the combined horizontal advective and evaporative cooling exceeds the downward adiabatic warming, thereby causing the net local cooling over most of the inner-core regions, but with the notable warming tendencies in the eye (Fig. 7d). Only at a few isolated places in the eyewall, some parcels may be possibly warmed to become buoyant.

The area-averaged heat budgets for the eyewall and hurricane system are given in Fig. 8, which shows the collective effects of deep convection on the large-scale environment. A deep layer of intense LHR occurs in the eyewall, from the top of the MBL to an 8-km altitude where the latent heating is peaked (Fig. 8a). A similar vertical profile appears when the eye region is included, but with substantial reduction in the peak heating, that is, from 42° to 12°C h^{-1} (cf. Figs. 8a,b). Horizontal advection tends to transport *potentially* warmer air outward in the supergradient outflow above the MBL (Fig. 8a). This advective warming has a bimodal distribution: one peak is associated with the LLOJ and the other in the upper-level outflow layer, both at a rate of >12°C h^{-1}. However, only one (upper level) advective warming peak appears after including the eye region (Fig. 8b). This warming peak, located about 4 km above the peak diabatic heating level, suggests the important role of the upper outflow layer in transporting warm air out of the storm. (The radial adiabatic warming above the LLOJ should be small due to the reduced radial pressure gradient.) The significant horizontal advective effects distinguish hurricanes from other types of MCSs, for example, as diagnosed by Yanai et al. (1973), Kuo and Anthes (1984), and Lin and Johnson (1996). In the MBL, horizontal advection transports *potentially* cooler air cyclonically inward (mostly associated with isothermal expansion toward the central lower pressure) that is nearly offset by the upward surface sensible heat flux [see the estimation related to Eq. (7) in Part II]. Regardless of how intense the diabatic heating and horizontal advection warming are, *the composite vertical advective cooling is almost balanced with the combined diabatic and horizontal advective effects,* leading to near-vanishing net local tendencies both in the eyewall and on the storm scale. This result reveals the significance of vertical motion in hurricanes in determining the heat budget and vertical heating profiles, which is in agreement with the conclusion obtained by the previous heat budget studies of MCSs mentioned earlier.

4. Moisture *q* budgets

In general, the vertical profiles and horizontal distributions of the moisture budgets are similar to those of the heat budgets, since their sources and sinks are related but are opposite in sign, as indicated by Eqs. (1) and (2), except in the MBL. Briefly, the Lagrangian moisture

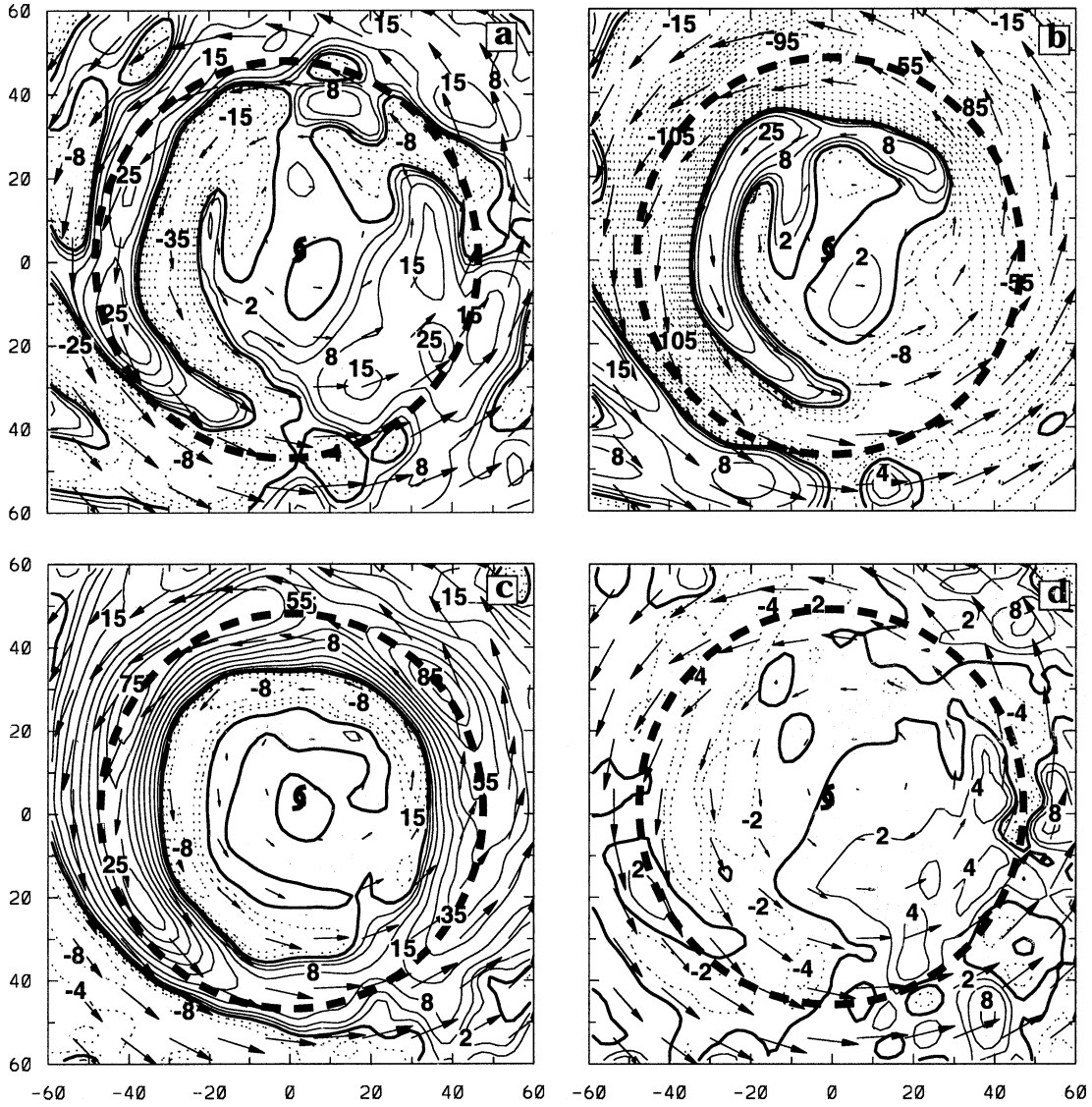

FIG. 7. As in Fig. 4 but for (a) the horizontal advection (θ_H); (b) the vertical advection (θ_v); (c) the latent heating rates ($d\theta/dt$); and (d) the local tendencies (θ_T) of potential temperature at $z = 8$ km. Solid (dashed) lines are positive (negative) values. The thick-dashed circle denotes the distribution of the updraft core.

budgets consist mainly of the moisture sources from the MBL with the peak near the RMW, and the moisture sinks associated with cloud condensation-deposition in the eyewall and spiral rainbands (Figs. 9a,b). The phase-change rates in the eyewall are so high that more than twice the local moisture content could be consumed in 1 h near the updraft core (i.e., $z \sim 5$–8 km) (cf. Figs. 1c and 9b). Clearly, the moisture source in the MBL, increasing toward the eyewall in proportion to the low-level swirling winds, provides the necessary latent energy for the development and maintenance of the storm. Horizontal and vertical diffusions tend to reduce the amplitude of deviation specific humidity (q') between the DN and UP axes, but increase it outside (cf. Figs. 9a and 1c). Note the positive tendencies inside the DN axis that represent the important upward transport of moisture from the MBL (Fig. 9a). However, the diffusive effects are generally one order of magnitude[1] smaller than the other terms in Eq. (1) (cf. Figs. 9a,c). In contrast to the moisture loss in the eyewall, phase changes result in the moisture gain in the spirally descending DN flow at the inner edge of the eyewall (due to the evaporation of cloud hydrometeors as they encounter the dry eye air) (Fig. 9b). This result shows further the role of sublimation–evaporation in enhancing the de-

[1] Comparing the diffusive to the phase-change rates along the DN axis could be misleading due to the aliasing problem in plotting them in such a radially narrow zone, as can be seen by comparing Figs. 3a and 6b.

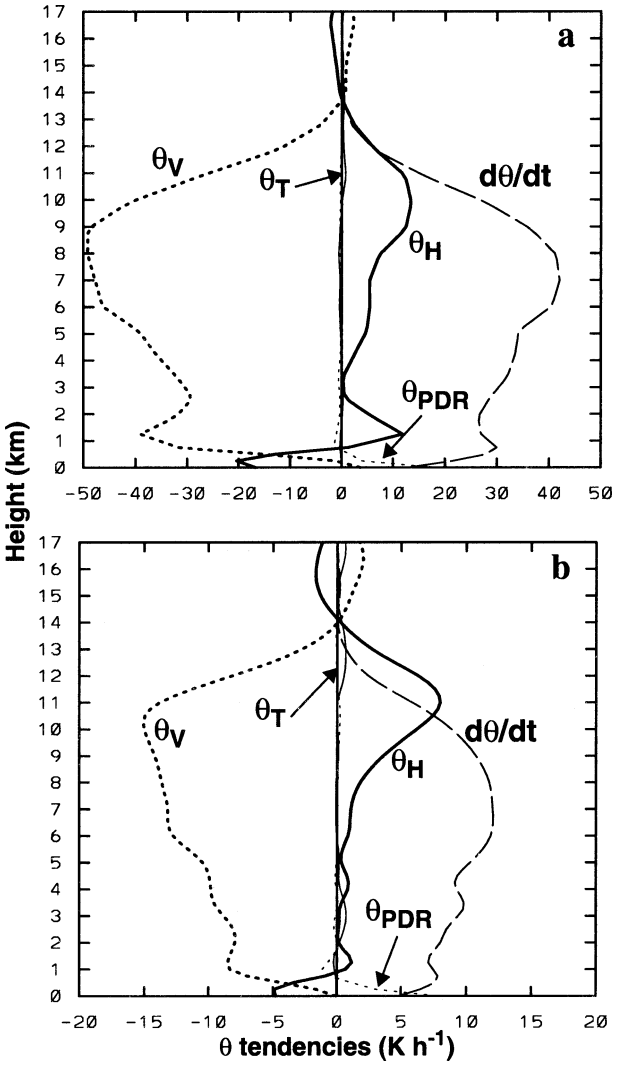

FIG. 8. Composite vertical profiles of the potential temperature θ budgets from the 56–57-h integration that are obtained by averaging them over (a) a conic annulus centered along the slanting surface shown in Fig. 5 (i.e., in the eyewall) with a width of 12 km; and (b) a cylindrical area centered at the min central pressure with a radius of 80 km. The θ-budget terms include the net diabatic heating rate ($d\theta/dt$), local tendency (θ_T), horizontal (θ_H) and vertical (θ_v) advection, and the PBL diffusion and radiative effects (i.e., $\theta_{PDR} = \theta_{BLD} + \theta_{RAD}$).

velopment of the penetrative downdrafts at the eyewall's inner edge.

In spite of the marked moisture loss by the phase changes, the air column could still maintain a near-saturated condition as a result of the upward transport of moisture in the eyewall updrafts and rainbands (cf. Figs.

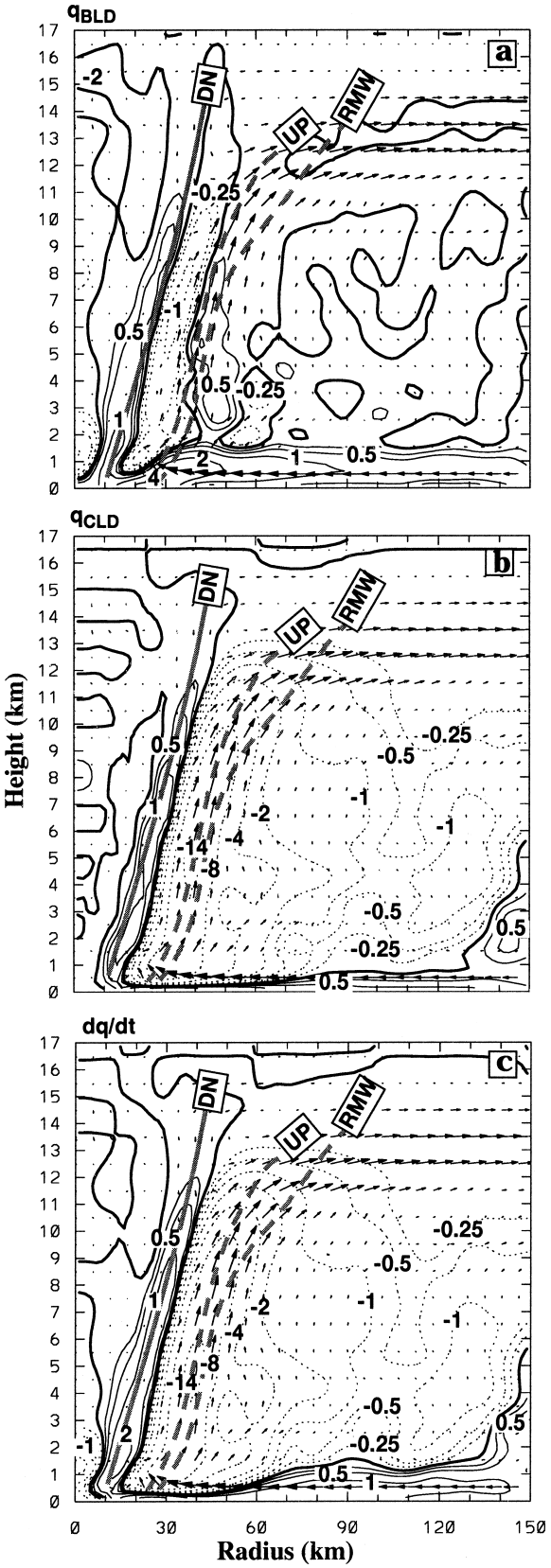

→

FIG. 9. As in Fig. 1 but for the specific humidity q budgets: (a) the PBL and diffusive processes (q_{BLD}); (b) in-cloud condensation rates (q_{CLD}); and (c) the net moisture tendency (dq/dt). They are contoured at 0, ±0.25, ±0.5, ±1, ±2, ±4, ±8, and ±14 g kg^{-1} h^{-1}.

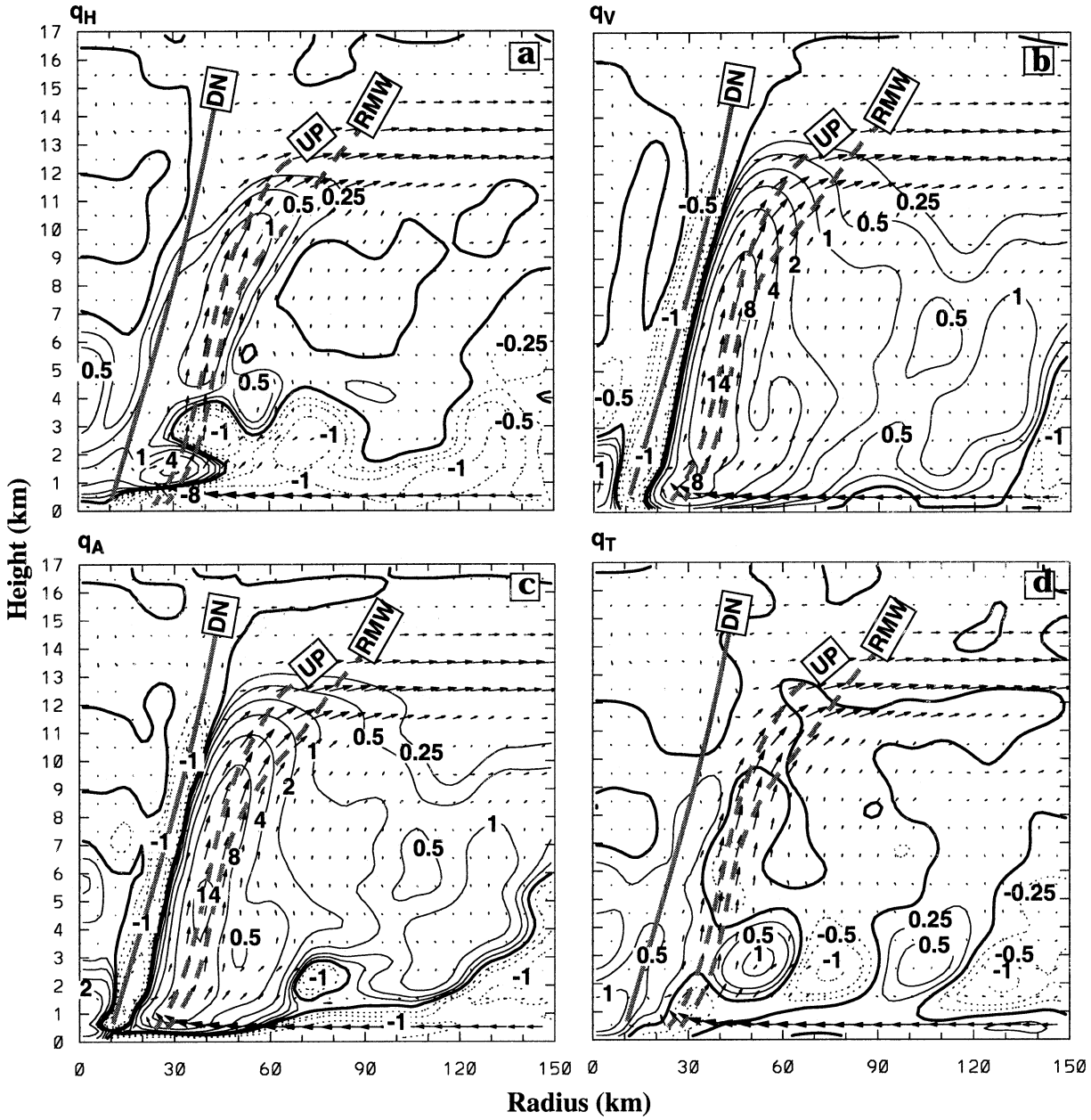

FIG. 10. As in Fig. 1 but for (a) the horizontal advection (q_H); (b) the vertical advection (q_v); (c) the total advection (q_A); and (d) the local tendency (q_T) of specific humidity. They are contoured at 0, ±0.25, ±0.5, ±1, ±2, ±4, ±8, and ±16 g kg^{-1} h^{-1}.

9c and 10b). Because of the near-saturated conditions, there is little storage of moisture in the eyewall (Fig. 10d). In contrast, in the MBL horizontal advection tends to transport the drier environmental air into the storm, and the more moist air from the moist core into the (outflow) eyewall (cf. Fig. 10a and 1c). However, the horizontal advective contributions to the moisture budgets are relatively small compared to the vertical advection in the eyewall, except in the LLOJ. Like in the θ budget, the total q advective rates are similar in magnitude but opposite in sign to the net q sources (cf. Figs. 9c and 10c). Nevertheless, one can still see the net moisture gain (a) at the inner edge of the eyewall (DN) where evaporation and the diffusion/boundary layer transport exceed the downward advective drying effect, and (b) in the eye's bottom 3-km-layer due likely to the Ekman pumping (Fig. 10d). As will be seen in the next section, the moisture gains are responsible for the development of higher-θe surfaces along the eye–eyewall interface.

5. Equivalent potential temperature θe budgets

Although θe is related to θ and q through Eqs. (1)–(3), the θe budgets are desirable for understanding (a)

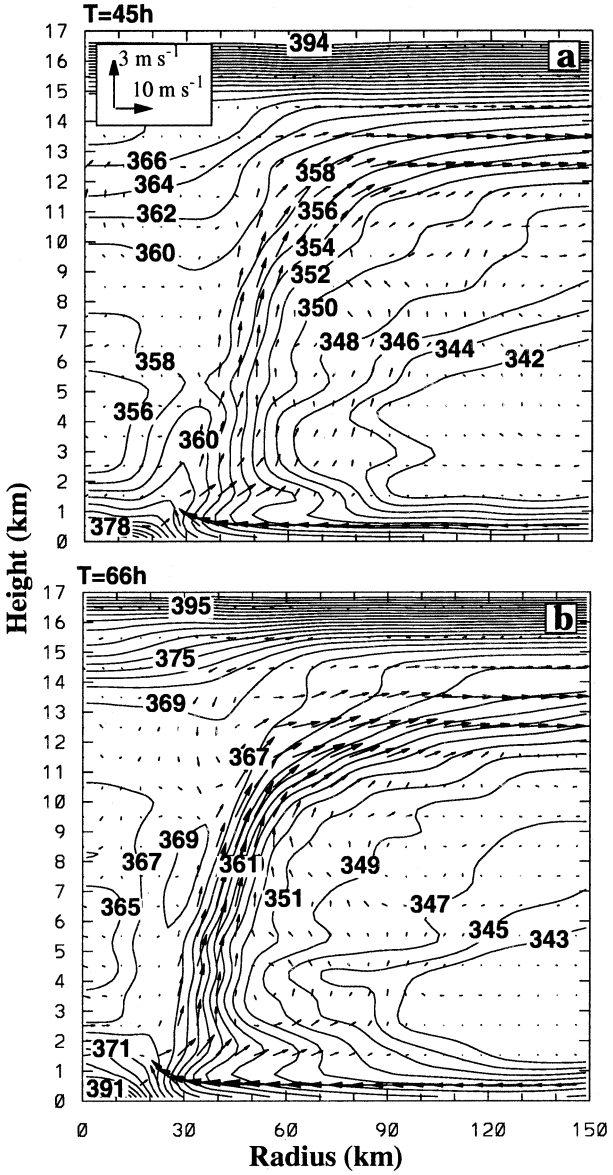

FIG. 11. The radius–height cross sections of the azimuthally averaged equivalent potential temperature θe at intervals of 2 K and in-plane flow vectors that are taken from (a) 45-h, and (b) 66-h integrations.

to what extent θe could be considered as a conserved variable; and (b) how the θe transport takes place in the inner-core regions of a hurricane. Specifically, Fig. 1d shows that the highest-θe surface appears at the inner edge DN rather than along the updraft core of the eyewall, with the lowest θe located at the eye center. These θe structures differ from those in typical MCSs whose core always coincides with that of high θe (e.g., Ogura and Liou 1980; Zhang and Cho 1992). Moreover, Figs. 11a, 1d and 11b show that the θe gradient across the eyewall intensifies from 10 K (25 km)$^{-1}$ to 18 K (25 km)$^{-1}$ during the 21-h integration. This intensification occurs as the penetrative θe values near the DN axis increases in amplitude (i.e., from 360 to 369 K), whereas the environmental θe values remain nearly unchanged during the model integration. Thus, one may ask: how does this higher-θe surface develop along the eye–eyewall interface where the upward motion is very weak? And how does the θe transport occur in the inner-core regions in the context of the eyewall updraft development?

To address the above questions, the radius–height cross sections of the θe budgets are given in Fig. 12. As mentioned before, the surface layer provides an important source of θe, which increases rapidly toward the RMW. We have estimated in Part II [see Eq. (7) related discussions therein] that the upward fluxes of surface latent and sensible heat and the isothermal expansion account roughly for 64%, 14%, and 22% of the total θe increase, respectively, as a parcel moves cyclonically from $R = 150$ km to the eye center in the surface layer. Horizontal diffusion above the MBL only acts to smooth the θe field, decreasing (increasing) it inward (outward) from the UP axis, and increasing it along the DN axis (Fig. 12a). The negative diffusive θe tendencies at the eye center, corresponding to positive θ tendencies in Fig. 2a and negative q tendencies in Fig. 9a, appear to be the result of Gibbs phenomenon due to the use of the fourth-order numerical diffusion scheme (Xue 2000). Nevertheless, their magnitudes are generally much smaller than those produced by the nonconservative physical processes given in Eq. (3). In contrast, the vertical turbulent mixing is pronounced in the vicinity of the LLOJ and along the DN axis below $z = 2$ km. Strictly speaking, θe is not conserved in the eyewall above the MBL due to the exclusion of deposition–sublimation and freezing–melting in the definition of θe (Fig. 12b). However, the peak cooling rate (> -8°C h^{-1}) associated with melting of precipitation, causing a local decrease of θe, occurs at the outer edge of the eyewall whereas inside it the cooling/warming rates are much smaller than the θe advective rates (cf. Figs. 12b and 13a,b). Thus, θe could still be considered as being *approximately* conserved in the eye/eyewall above the MBL even though deposition–sublimation and freezing–melting occur. We may speculate that the melting impact on the conservation of θe could be pronounced when the eyewall is near upright.

With the near-conservative property of θe, we may study the θe transport in the eyewall qualitatively in terms of advective processes. Figure 13a shows that horizontal advection in the MBL inflow (or in outer regions) transports lower-θe air into the storm (or rainbands), more than offsetting the θe source from the surface layer. Clearly, an excess of θe has to be generated from the underlying warm ocean to overcompensate this negative advective effect if the hurricane were to intensify. On the other hand, *upward motion tends to advect the MBL higher-*θe *air upward in outer regions or in rainbands, similar to the case of typical MCSs, but reduces the* θe *magnitude in the eyewall* (Fig.

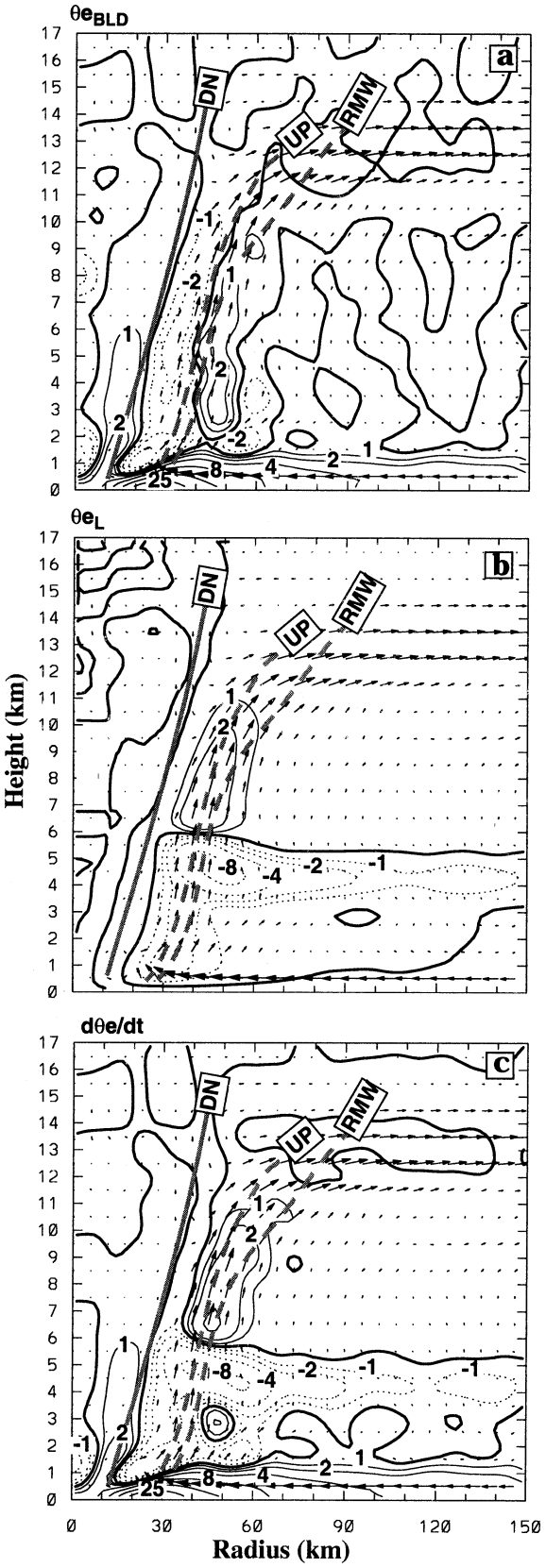

13b). The negative tendencies are more pronounced in the LLOJ and the upper portion of the eyewall, thus intensifying the radial θe gradient across the eyewall. Like the θ and q budgets, it is the horizontal (outflow) advection that is responsible for transferring higher-θe air from the eyewall's inner edge outward, counteracting the negative vertical θe advection in the eyewall. At the inner edge (i.e., in the DN zone), the upper return inflow and its subsequent descent tend to transport the upper-level higher-θe (or high θ) air downward, whereas the LLOJ (and the weak updrafts near the inner edge) transports some high-θe air from the bottom eye region into the eyewall (see Figs. 11 and 13b). Note the positive radial advective tendencies at the eye center that appear to be generated due to the fact that the upper-level vortex circulations are not centered with the minimum surface pressure (cf. Figs. 13a, 4, and 7). This seems to help explain why θe at the eye center tends to increase with time, as shown in Figs. 11a, 1d, and 11b. It should be pointed out that this phenomenon was previously speculated (in Part II) to result from the use of numerical diffusion.

The net results are excess θe tendencies in the MBL, negative θe tendencies in the eyewall but positive θe tendencies at the inner edge (Fig. 13c). Although the net tendencies are small residues between large terms, they appear to make sense in terms of θe transport for an intensifying hurricane. For instance, the weak negative tendency in the eyewall reveals again the importance of slantwise updrafts in transporting higher-θe air from the MBL. The net positive θe tendency at the inner edge is consistent with the local θe increases, for example, from 358 K at $t = 45$ h to 369 K at $t = 66$ h (Figs. 11a,b). To our knowledge, this positive θe tendency has not been explored in the literature, and it appears to be caused by both the bottom–up processes near the top of the LLOJ and the top–down processes along the DN axis (Fig. 13b). They are also evidenced by the upward bulge, downward dip, and vertical merging of θe surfaces (see Figs. 1d and 11a,b). Part of this higher-θe air will enter (or recycle into) the eyewall by the supergradient outflow. This result supports further our finding, given in Part III (see Fig. 4 therein), that the eyewall updrafts are enhanced (weakened) in the outflow (inflow) regions due to the radially advected positive (negative) θe perturbations.

6. Summary and conclusions

In this study, we have examined the inner-core thermodynamics of a hurricane, through the analyses of

←

FIG. 12. As in Fig. 1 but for the equivalent potential temperature θe sources/sinks: (a) the PBL and diffusive processes (θe_{BLD}); (b) in-cloud latent heating associated with fusion and freezing–melting (θe_L); and (c) the net θe source ($d\theta e/dt$). They are contoured at 0, ± 1, ± 2, ± 4, ± 8, ± 15, and ± 25 K h^{-1}.

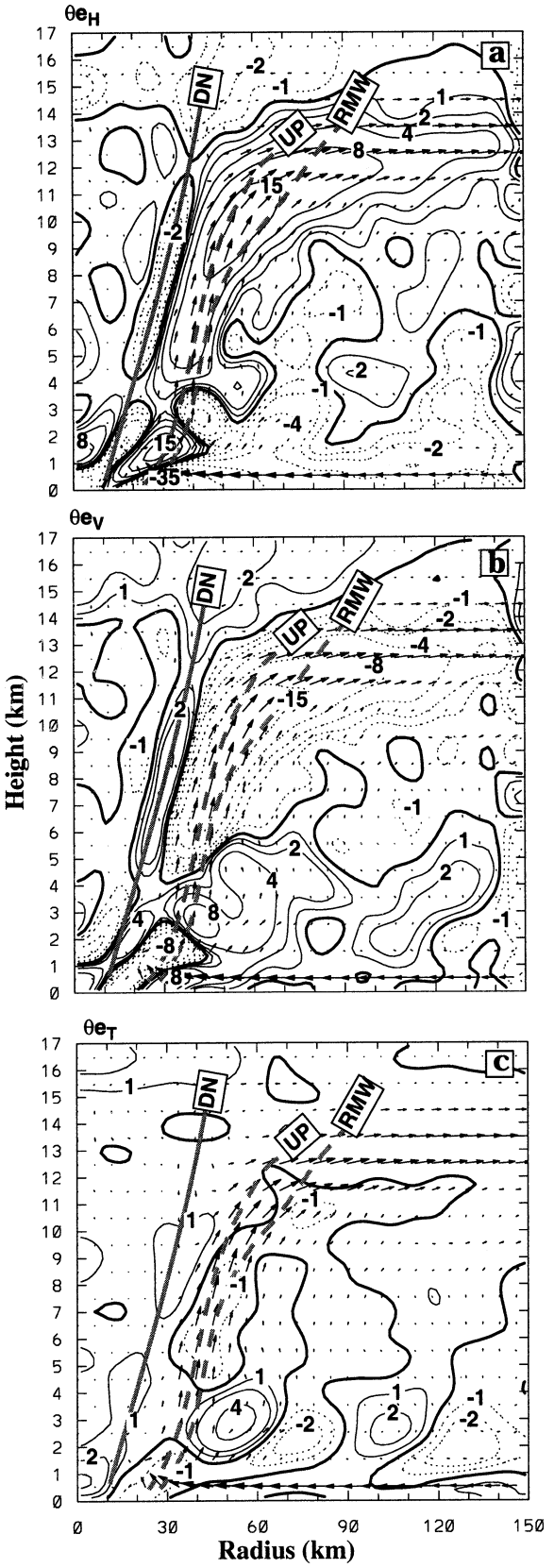

heat, moisture, and equivalent potential temperature budgets, using a high-resolution ($\Delta x = 6$ km), nonhydrostatic, fully explicit simulation of Hurricane Andrew (1992) during its mature (or intensifying) stage. Important results are summarized as follows:

- It is found from the potential temperature budgets that the heat energy is dominated by LHR in the eyewall, sublimative–evaporative cooling at the eye–eyewall interface and the upward surface fluxes of sensible (and latent) heat from the underlying warm ocean. The intensity of LHR rates in the eyewall depends on whether latent heat is released in the radial inflow (e.g., <10°C h^{-1}) or outflow (e.g., >100°C h^{-1}) regions. The LHR rates in the inflow regions decrease from the eyewall core inward and become negative near the eye–eyewall interface due to the meeting of the inward-advected cold cloudy air from the eyewall with the warm-dry air in the eye. Although most of the latent heating in the eyewall is generated by warm-rain processes, depositional growth and freezing (>25°C h^{-1}) tends to shift the heating maximum to a slightly higher level and the heating effects into a deeper layer.
- It is shown that in the (supergradient) mean outflow the radial θ advection tends to advect warmer air in the core regions to strengthen the eyewall updrafts, which is more pronounced in the upper outflow layer, thereby weakening the thermal gradient across the eyewall. In the height–azimuth cross section, however, the presence of radial inflows gives rise to intense θ advective cooling that accounts for the initiation and maintenance of penetrative downdrafts at the eye–eyewall interface; the latter are only enhanced by the sublimative–evaporative cooling. Vertical advection produces weak adiabatic warming in the eye, partly by the descending air mass at the eye–eyewall interface from the return inflow above the upper outflow layer, and intense adiabatic cooling in the eyewall whose rates offset the sum of radial advective warming and total diabatic heating. This explains why little net warming could be found in the eyewall in spite of intense LHR. Thus, we may state that the vertical thermal advection accounts for net cooling of the eyewall, peaked in the updraft core, and for a warm core in the eye such that the thermal gradient across the eyewall increases with time, whereas the radial thermal advection tends to reduce the thermal gradient. It is the radial inflow that is mostly responsible for initiating the penetrative downdrafts at the eye–eyewall interface.
- Composite heat budgets show that vertical advective

←

FIG. 13. As in Fig. 1 but for (a) the horizontal advection (θe_H); (b) the vertical advection (θe_v); and (c) the local tendency (θe_T) of equivalent potential temperature θe. They are contoured at 0, ± 1, ± 2, ± 4, ± 8, ± 15, ± 25, and ± 35 K h^{-1}.

cooling is nearly balanced with the combined diabatic and horizontal advective heating effects, leading to near-vanishing net tendencies both in the eyewall and on the storm scale in a storm-relative framework. The composite vertical profile of latent heating in the inner-core region is similar to that of vertical motion, except in the upper outflow layer where radial advective warming dominates. This reveals the significance of vertical motion in hurricanes in determining the heat budget and vertical heating profiles.

- The vertical profiles and horizontal distributions of the moisture budgets are similar to those of the heat budgets, since their sources and sinks are related but are opposite in sign, except in the MBL where the upward surface moisture flux provides the necessary latent energy for the convective development in the eyewall. The moisture budgets exhibit the dominant upward transport of moisture in the eyewall updrafts and rainbands so that the eyewall is nearly saturated. The moisture budgets also show the importance of the LLOJ in transporting moisture into the eyewall from the bottom eye regions.
- It is found that θe could be considered as an approximately conserved variable above the MBL even in the presence of deposition–sublimation and freezing–melting; this appears to be related to the slantwise orientation of the eyewall. The slantwise advection accounts for the transport of most higher-θe air from the MBL into the eyewall. Of interest is the continued development of higher-θe surfaces at the eye–eyewall interface that is closely related to the intensifying θe gradient across the eyewall and enhancement of the eyewall convection. This development results from the downward transport of higher-θe (or θ) air from the upper troposphere by the penetrative downdrafts (in the inflow regions) and the upward transport of higher-θe air from the eye's MBL by the LLOJ (in the outflow regions). Hence, we may conclude that the hurricane eyewall is thermodynamically maintained by the upward surface flux of higher-θe air from the underlying warm ocean, the descent of higher-θe air in the upper troposphere, and the recycling of some warmed-eye air in the outflow regions.

Note that the above budget results are obtained from an explicit simulation of a hurricane in which there are some deficiencies due partly to the use of various parameterizations in the cloud microphysics and MBL schemes and partly to the use of the 6-km grid size that is still too coarse to resolve deep convection in the eyewall. Note also that the results presented herein may be more suitable for mature hurricanes with strong intensity; caution may need to be taken when they are applied to incipient, or rapidly decaying storms. Nevertheless, many agreements between the simulated and the observed Andrew presented in Part I led us to our belief that the basic conclusions presented herein are relevant to real tropical storms.

Acknowledgments. This work was supported by the NSF grant ATM-9802391, the NASA Grant NAG-57842, and the ONR Grant N00014-96-1-0746. The computations were performed at the National Center for Atmospheric Research, which is sponsored by the National Science Foundation.

REFERENCES

Anthes, R. A., 1982: *Tropical Cyclones—Their Evolution, Structure, and Effects, Meteor. Monogr.*, No. 41, Amer. Meteor. Soc., 208 pp.

Bolton, D., 1980: The computation of equivalent potential temperature. *Mon. Wea. Rev.,* **108,** 1046–1053.

Chen, Y., and M. K. Yau, 2001: Spiral bands in a simulated hurricane. Part I: Vortex Rossby wave verification. *J. Atmos. Sci.,* **58,** 2128–2145.

Dudhia, J., 1993: A nonhydrostatic version of the Penn State–NCAR Mesoscale Model: Validation tests and simulation of an Atlantic cyclone and cold front. *Mon. Wea. Rev.,* **121,** 1493–1513.

Gallus, W. A., Jr., and R. H. Johnson, 1991: Heat and moisture budgets of an intense midlatitude squall line. *J. Atmos. Sci.,* **48,** 122–146.

Gamache, J. F., R. A. Houze, and F. D. Marks, 1993: Dual-aircraft investigation of the inner core of Hurricane Norbert. Part III: Water budget. *J. Atmos. Sci.,* **50,** 3221–3243.

Grell, G. A., J. Dudhia, and D. R. Stauffer, 1995: A description of the fifth generation Penn State/NCAR mesoscale model (MM5). NCAR Tech. Note NCAR/TN-398+STR, 138 pp.

Hawkins, H. F., and D. T. Rubsam, 1968: Hurricane Hilda, 1964. II: Structure and budgets of the hurricane on Oct. 1, 1964. *Mon. Wea. Rev.*, **96,** 617–636.

——, and S. M. Imbembo, 1976: The structure of a small, intense hurricane—Inez 1966. *Mon. Wea. Rev.,* **104,** 418–442.

Johnson, R. H., and G. S. Young, 1983: Heat and moisture budgets of tropical anvil clouds. *J. Atmos. Sci.,* **40,** 2138–2147.

Jorgensen, D. P., 1984: Mesoscale and convective scale characteristics of nature hurricanes. Part II: Inner core structure of Hurricane Allen (1980). *J. Atmos. Sci.,* **41,** 1287–1311.

Krishnamurti, T. N., K. S. Yap, and D. K. Oosterhof, 1991: Sensitivity of tropical storm forecast to radiative destabilization. *Mon. Wea. Rev.,* **119,** 2176–2205.

Kuo, Y.-H., and R. A. Anthes, 1984: Mesoscale budgets of heat and moisture in a convective system over the central United States. *Mon. Wea. Rev.,* **112,** 1482–1497.

Kurihara, Y., and M. A. Bender, 1982: Structure and analysis of the eye of a numerically simulated tropical cyclone. *J. Meteor. Soc. Japan,* **60,** 381–305.

Lin, X., and R. H. Johnson, 1996: Heating, moistening, and rainfall over the western Pacific warm pool during TOGA COARE. *J. Atmos. Sci.,* **53,** 3367–3383.

Liu, Y., D.-L., Zhang, and M. K. Yau, 1997: A multiscale numerical study of Hurricane Andrew (1992). Part I: Explicit simulation and verification. *Mon. Wea. Rev.,* **125,** 3073–3093.

——, ——, and ——, 1999: A multiscale numerical study of Hurricane Andrew (1992). Part II: Kinematics and inner-core structures. *Mon. Wea. Rev.*, **127,** 2597–2616.

Mapes, B. E., and R. A. Houze Jr., 1995: Diabatic divergence profiles in western Pacific mesoscale convective systems. *J. Atmos. Sci.,* **52,** 1807–1828.

Montgomery, M. T., and R. J. Kallenbach, 1997: A theory for vortex Rossby waves and its application to spiral bands and intensity changes in hurricanes. *Quart. J. Roy. Meteor. Soc.,* **123,** 435–465.

Ogura, Y., and M.-T. Liou, 1980: The structure of a midlatitude squall line: A case study. *J. Atmos. Sci.,* **37,** 553–567.

Olson, W. S., C. D. Kummerow, Y. Hong, and W.-K. Tao, 1999: Atmospheric latent heating distributions in the Tropics derived

from satellite passive microwave radiometer measurements. *J. Appl. Meteor.*, **38,** 633–664.
Puri, K., and M. J. Miller, 1990: The use of satellite data in the specification of convective heating for diabatic initialization and moisture adjustment in numerical weather prediction models. *Mon. Wea. Rev.,* **118,** 67–93.
Rodgers, E. B., W. S. Olson, V. M. Karyampudi, and H. F. Pierce, 1998: Satellite-derived latent heating distribution and environmental influences in Hurricane Opal (1995). *Mon. Wea. Rev.*, **126,** 1229–1247.
——, ——, J. Halverson, J. Simpson, and H. Pierce, 2000: Environmental forcing of Supertyphoon Paka's (1997) latent heat structure. *J. Appl. Meteor.*, **39,** 1983–2006.
Tao, W.-K., and J. Simpson, 1993: The Goddard cumulus ensemble model. Part I: Model description. *Terr. Atmos. Oceanic Sci.,* **4,** 35–72.
——, ——, S. Lang, M. McCumber, R. Adler, and R. Penc, 1990: An algorithm to estimate the heating budget from vertical hydrometeor profiles. *J. Appl. Meteor.*, **29,** 1232–1244.
Willoughby, H. E., 1998: Tropical cyclone eye thermodynamics. *Mon. Wea. Rev.,* **126,** 3053–3067.
Xue, M., 2000: High-order monotonic numerical diffusion and smoothing. *Mon. Wea. Rev.,* **128,** 2853–2864.
Yanai, M., S. Esbensen, and J.-H. Chu, 1973: Determination of bulk properties of tropical cloud clusters from large-scale heat and moisture budgets. *J. Atmos. Sci.,* **30,** 611–627.
Yang, S., and E. A. Smith, 1999: Four-dimensional structure of monthly latent heating derived from SSM/I satellite measurements. *J. Climate,* **12,** 1016–1037.
Zhang, D.-L., 1989: The effect of parameterized ice microphysics on the simulation of vortex circulation with a mesoscale hydrostatic model. *Tellus,* **41A,** 132–147.
——, and J. M. Fritsch, 1988: Numerical sensitivity experiments of varying model physics on the structure, evolution and dynamics of two mesoscale convective systems. *J. Atmos. Sci.,* **45,** 261–293.
——, and H.-R. Cho, 1992: The development of negative moist potential vorticity in the stratiform region of a simulated squall line. *Mon. Wea. Rev.,* **120,** 1322–1341.
——, and N. Bao, 1996: Oceanic cyclogenesis as induced by a mesoscale convective system moving offshore. Part I: A 90-h real-data simulation. *Mon. Wea. Rev.,* **124,** 1449–1469.
——, Y. Liu, and M. K. Yau, 2000: A multiscale numerical study of Hurricane Andrew (1992). Part III: Dynamically induced vertical motion. *Mon. Wea. Rev.,* **128,** 3772–3788.
——, ——, and ——, 2001: A multiscale numerical study of Hurricane Andrew (1992). Part IV: Unbalanced flows. *Mon. Wea. Rev.,* **129,** 92–107.